Biomaterials 293 (2023) 121983

Contents lists available at ScienceDirect

Biomaterials

journal homepage: www.elsevier.com/locate/biomaterials

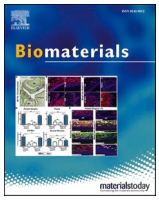

Human iPS-derived blood-brain barrier model exhibiting enhanced barrier properties empowered by engineered basement membrane

Jeong-Won Choi [a,1], Jaeseung Youn [b,1], Dong Sung Kim [b,c,d,**], Tae-Eun Park [a,*]

[a] Department of Biomedical Engineering, College of Information and Biotechnology, Ulsan National Institute of Science and Technology (UNIST), Ulsan, 44919, Republic of Korea
[b] Department of Mechanical Engineering, Pohang University of Science and Technology (POSTECH), Pohang, 37673, Republic of Korea
[c] Department of Chemical Engineering, Pohang University of Science and Technology (POSTECH), Pohang, 37673, Republic of Korea
[d] Institute for Convergence Research and Education in Advanced Technology, Yonsei University, Seoul, 03722, Republic of Korea

ARTICLE INFO

Keywords:
Blood-brain barrier
Basement membrane
Hydrogel membrane
Electrospun nanofibers
Ischemic stroke modeling

ABSTRACT

The basement membrane (BM) of the blood-brain barrier (BBB), a thin extracellular matrix (ECM) sheet underneath the brain microvascular endothelial cells (BMECs), plays crucial roles in regulating the unique physiological barrier function of the BBB, which represents a major obstacle for brain drug delivery. Owing to the difficulty in mimicking the unique biophysical and chemical features of BM in in vitro systems, current in vitro BBB models have suffered from poor physiological relevance. Here, we describe a highly ameliorated human BBB model accomplished by an ultra-thin ECM hydrogel-based engineered basement membrane (nEBM), which is supported by a sparse electrospun nanofiber scaffold that offers *in vivo* BM-like microenvironment to BMECs. BBB model reconstituted on a nEBM recapitulates the physical barrier function of the *in vivo* human BBB through ECM mechano-response to physiological relevant stiffness (~500 kPa) and exhibits high efflux pump activity. These features of the proposed BBB model enable modelling of ischemic stroke, reproducing the dynamic changes of BBB, immune cell infiltration, and drug response. Therefore, the proposed BBB model represents a powerful tool for predicting the BBB permeation of drugs and developing therapeutic strategies for brain diseases.

1. Introduction

The primary function of the blood-brain barrier (BBB) is the maintenance of brain homeostasis by controlling the entry of molecules into the brain. The BBB is composed of brain microvascular endothelial cells (BMECs) that line the cerebral capillaries together with the surrounding basement membrane (BM), pericytes, and astrocytes. This creates a unique microenvironment that regulates the physical and metabolic barrier functions of the BBB [1]. The tight junction integrity of BMECs creates a strong paracellular barrier, which allows the tight regulation of the movement of molecules between the blood and brain [1]. The multi-specific efflux pumps belonging to the ATP-binding cassette (ABC) transporter superfamily, expressed at the blood-facing BMECs, prevent the uptake of lipophilic molecules into the brain [2]. These features of the BBB hinder brain drug delivery, which makes the BBB a rate-limiting factor in central nervous system (CNS) drug development.

There have been many advancements in the modeling of the human BBB to evaluate the effects of toxic compounds by the monitoring barrier integrity and examination of the ability of brain drugs to cross the BBB [3,4]. Since the primary function of the BBB is to regulate and separate the blood and brain as distinct physiological compartments, the strategy to build relevant *in vitro* models usually involves the compartmentalization of different environments. Most BBB models reconstructed on the Transwell inserts and microfluidic devices utilize physical interfaces including semi-permeable porous membranes composed of synthetic polymers, such as polyester, polyethylene terephthalate (PET) [5,6], polycarbonate (PC) [7], or polydimethylsiloxane (PDMS) [8] usually called as a synthetic membrane. Generally, a BMEC monolayer is formed on a synthetic membrane, whereas the astrocytes and pericytes are cultured on the other side of the membrane or in a different chamber to biochemically support the barrier function of BMECs [5,6,8]. To enhance the endogenous intercellular communications of BMECs with

* Corresponding author.
** Corresponding author. Department of Mechanical Engineering, Pohang University of Science and Technology (POSTECH), Pohang, 37673, Republic of Korea.
E-mail addresses: smkds@postech.ac.kr (D.S. Kim), tepark@unist.ac.kr (T.-E. Park).
[1] These authors contributed to this work equally.

https://doi.org/10.1016/j.biomaterials.2022.121983
Received 13 February 2022; Received in revised form 17 October 2022; Accepted 22 December 2022
Available online 23 December 2022

astrocytes and pericytes, recent studies have focused on developing functional polymeric porous membranes with submicron thickness [9–11].

However, these approaches often ignore the importance of BMs where cell phenotypes are regulated by the interaction between endothelial cells and the extracellular matrix (ECM). The BM is a continuous layer of approximately 20 nm–3 μm thickness [12], which appears as lightly matted feltworks of fine fibrils with a diameter of approximately 3–4 nm [13]. BMs are mainly composed of ECM proteins, such as type IV collagen, fibronectin, and laminin [12,14,15]. Young's modulus of BM has been reported in a broad range spanning from ~kPa to ~MPa [16] due to the complex challenges in measuring the mechanical characteristics of the biological sample. However, it has been often presented in the kPa range (~500 kPa) [15] according to many studies [17–21]. They not only provide a structural scaffold to support endothelial cells but also regulate cellular properties and functions through their unique biophysical and biochemical properties [22]. Particularly, BM stiffness plays an important role by regulating gene expression in response to mechanical cues by virtue of links between the cytoskeleton and ECM components via adhesion receptors [22]. The chemical cues provided by ECM proteins in a BM also influence cellular phenotypes and behaviors through the integrin-mediated cell-ECM interaction [23]. To date, several approaches have been made to fabricate *in vitro* BMs to provide these specialized BM environments to an *in vitro* BBB model [24–27], although the recapitulation of both biophysical and biochemical features of the BM of the BBB remains unrealized.

ECM coating on a synthetic membrane has been widely used as a simple method to provide BM-like biochemical cues to BMECs [23,28]. However, this approach disregards the biophysical cues of BM owing to the four orders of magnitude differences in Young's modulus between synthetic membrane (e.g., PET is ~2 GPa) [22] and *in vivo* BM (250–500 kPa) [15]. Therefore, BMECs grown on stiff synthetic membranes are not subjected to the physical forces that they endure in the body, exhibiting biological responses not relevant to *in vivo*, and resulting in diminished barrier integrity [24,29]. To address these problems, ECM hydrogels have emerged as a promising approach to offer both BM-like stiffness and ECM-mediated biochemical cues. Several previous reports have revealed that BBB models constructed on ECM hydrogel-based culture platforms show enhanced recapitulation of cellular phenotypes and barrier function depending on ECM composition [27,30] and hydrogel stiffness [24,27,31,32]. However, despite the advantages of ECM hydrogels as *in vitro* BMs, their greater thickness (over 100 μm) compared to that of *in vivo* BM (20 nm–3 μm) considerably increases the diffusion time of molecules. Furthermore, it requires laborious steps to collect the samples that are diffused into the thick ECM hydrogel followed by penetration of the BMEC layer, which might not be suitable for high-throughput *in vitro* drug permeability test or cell transmigration assay [33]. As such, we reasoned that a BBB model constructed on an ultra-thin and free-standing ECM hydrogel membrane would hold a promising potential for resembling the biophysical/chemical features of *in vivo* BM as well as versatile applications such as prediction of drug permeation and cell transmigration across the BBB.

This study investigates the development of an enhanced human *in vitro* BBB model exhibiting *in vivo*-like physiological barrier functions based on a nanofiber-assisted ultra-thin ECM hydrogel-based engineered basement membrane, named nEBM. The nEBM can potentially provide a BM-like environment to the human induced pluripotent stem cell-derived BMECs (iPS-BMECs) based on not only *in vivo* level of Young's modulus (~500 kPa) and BM-like ECM compositions but also very small thickness and high permeability. The nEBM could be substantially integrated into a well insert similar to the Transwell insert, which allowed versatile BBB co-culture and *in vitro* permeability assays. The enhanced BBB model further led to a model feature of acute ischemic stroke, proving useful for a better understanding of the pathophysiological mechanisms involved in the BBB-related diseases.

2. Results

2.1. Nanofiber scaffold-supported, soft ECM hydrogel membrane

A critical limitation of conventional synthetic membranes is the ~10 to ~10^4 times higher stiffness compared to native BM, which eventually causes abnormal cellular phenotypes *in vitro*. However, it remains technically challenging to generate a thin membrane composed of soft materials, such as ECM hydrogels, in a free-standing configuration. A key strategy to achieve a free-standing and *in vivo*-BM like soft membrane in this study was the use of soft ECM hydrogels with a specially designed scaffold that stably and reliably supports ECM hydrogel in a free-standing manner while minimizing compromise to ECM hydrogel stiffness. An ultra-thin electrospun nanofiber scaffold was employed, which has the potential to provide desired mechanical and physical properties for supporting ECM hydrogels. Finally, the Young's modulus of ECM hydrogels with the nanofiber scaffold could be tuned in the order of 100 kPa.

A highly porous, ultra-thin, and free-standing silk fibroin/polycaprolactone (SF/PCL) nanofiber scaffold exhibiting a high affinity toward ECM proteins was fabricated through an electrospinning process. Briefly, sparsely distributed SF/PCL nanofibers were deposited on a hollow-cylindrical metal collector in a free-standing configuration. The SF/PCL nanofiber scaffold was then transferred and conformally integrated on a polystyrene (PS) well insert with no membrane through thermal fusion bonding between the PS insert and the SF/PCL nanofibers, not requiring additional adhesive or clamping device. Type I collagen was coated in and on the SF/PCL nanofiber scaffold to fill the space between the sparsely distributed nanofibers with numerous collagen nanofibrils while maintaining the ultra-thin structure of the nanofiber scaffold. Subsequently, both type IV collagen and fibronectin were coated on the surface formed by type I collagen and the SF/PCL nanofiber scaffold (Fig. S1), thereby generating a nEBM-integrated well insert (hereafter called a nEBM insert) (Fig. 1a). While the commercial PET membrane possessed a flat surface with nanopores, distributed at a spacing of approximately 10–100 μm, the nEBM exposed a naturally porous and nanofibrous topography composed of SF/PCL nanofibers and collagen nanofibrils (Fig. 1b). The present nEBM was mainly composed of ECM-derived hydrogels containing key ECM proteins of BM, such as type IV collagen and fibronectin, supported by an ultra-thin and highly porous nanofiber scaffold. The nEBM exhibited unique biophysical properties, distinct from the commercial PET membrane, exhibiting a significantly lower Young's modulus (554.78 ± 33.10 kPa against ~2 GPa of PET; Fig. 1c), a smaller thickness (~5 μm against ~10 μm of PET) (Fig. 1b and d), and the higher apparent permeability (P_{app}) of 3 and 10 kDa FITC-Dextran (Fig. 1e and f).

To the best of author's knowledge, a Young's modulus similar to that of the BM (~500 kPa) has not been achieved so far for membrane with thickness of <10 μm while satisfying the sufficient mechanical strength required to sustain its free-standing structure supporting both a cell monolayer and the culture medium. The results suggest that the nEBM could be the first membrane providing not only BM-like stiffness but also BM-like biochemical cues to BMECs. Furthermore, the nEBM seems closer to the BM compared to the PET membrane in terms of nanofibrous topography, small thickness, and high permeability.

2.2. Reconstruction of the human BBB on a nEBM with greater physical barrier function

To verify the enhancement of physiological relevance of the BBB culture by the nEBM, a human BBB was reconstructed through a culture of hypoxia-enhanced iPS-BMECs [6] on a nEBM insert and a mixture of human primary astrocytes and pericytes placed at the bottom of the 24-well plate to assist the functional maturation of iPS-BMECs (Fig. 2a). Electron microscopic analysis confirmed that the nEBM successfully supported the iPS-BMECs and iPS-BMEC monolayer was formed only on

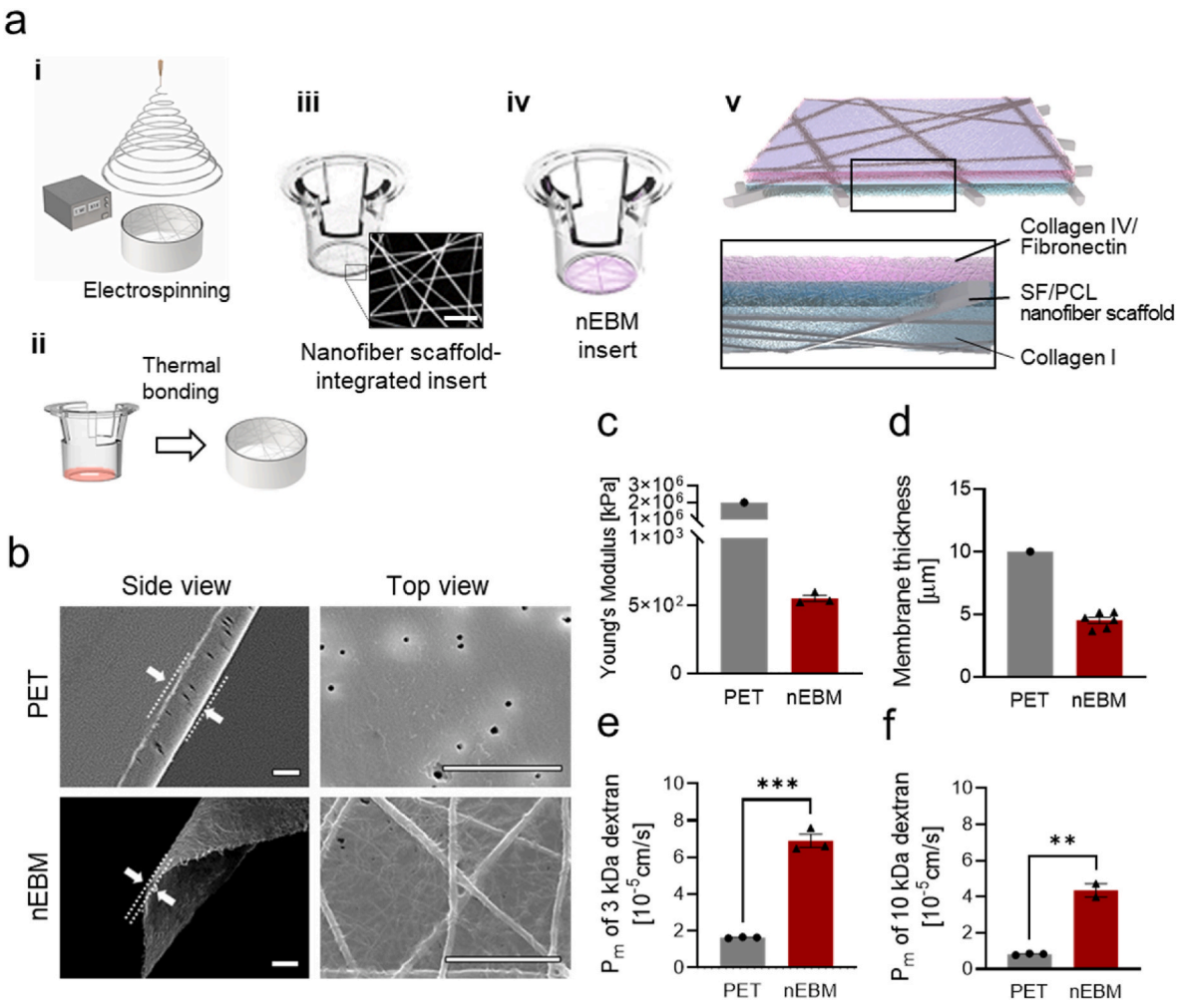

Fig. 1. An ultra-thin ECM hydrogel membrane supported by a sparse electrospun nanofiber skeleton, composed of silk fibroin (SF)/polycaprolactone (PCL)—Nanofiber-assisted ECM hydrogel-based engineered basement membrane (nEBM). (a) Schematic illustration of the nEBM fabrication process: (i) Electrospinning set-up for the fabrication of free-standing and ultra-thin SF/PCL nanofiber scaffolds (ii) Nanofiber scaffold integration with the well insert through thermal bonding (iii) Prepared nanofiber scaffold-integrated well insert. Scale bar = 10 μm. (iv) nEBM insert with blood-brain barrier extracellular matrix hydrogels. (b) Scanning electron microscopy (SEM) images of commercial polyethylene terephthalate (PET) membrane and nEBM: Cross-section view and Top view. Scale bar = 10 μm. (c) Young's modulus of PET membrane and nEBM. (d) Membrane thickness of PET membrane and nEBM. (e–f) Membrane permeability coefficients of 3 kDa and 10 kDa dextran across PET membrane and nEBM. These results are presented as the mean ± standard error of mean (s.e.m.) (n = 3). For statistical analysis, an unpaired *t*-test was performed (**P < 0.01; ***P < 0.001).

the apical side of nEBM (Fig. S2). When analyzing the number of DAPI-stained nuclei of iPS-BMECs, no difference in final cell density was observed between the iPS-BMECs cultured on the nEBM and PET membrane (Fig. S3).

A primary function of the BBB is to provide an effective physical barrier due to the tight junction protein interactions between adjacent iPS-BMECs [26,34]. Therefore, the physical barrier function of the proposed BBB model was comparatively studied with that developed on PET membranes. The TEER value of a BBB model developed on the nEBM together with astrocytes and pericytes was similar to that of an *in vivo* BBB (> 2000 Ω cm^2) [26], attaining 2600 Ω cm^2 on day three, which was significantly higher than that developed on the PET membrane (Fig. 2b and Table S1). This result was verified using fluorescent-labeled 3 and 10 kDa dextrans to measure the barrier integrity (Fig. 2c and d). The apparent permeability (P_{app}) of dextran in the BBB culture developed on the nEBM was significantly lower than that developed on the PET membrane on day 3, and it correlated with the size of tracers (5×10^{-8} and 4×10^{-9} cm s^{-1} for 3 and 10 kDa dextran, respectively). The P_{app} values obtained from this static BBB model appeared highly comparable to that of the hypoxic-stimulated microfluidic BBB chip reported previously by the authors [6]. In addition, we tested if nEBM-induced enhancement of barrier property is observed in other endothelial cell source. Similarly, when human umbilical vein endothelial cells (HUVEC) were cultured on the nEBM, they displayed higher TEER value than that developed on the PET membrane, even though TEER was one magnitude lower than that of iPS-BMECs (Fig. S4).

The confocal fluorescence microscopic analysis revealed a distinct endothelial monolayer on the nEBM with effectively developed tight junctions expressing ZO-1, Claudin-5, and Occludin along the lateral borders, and the GLUT-1 expression on the apical side of the iPS-BMECs. The analysis did not identify differences in the expression and localization of those marker proteins between the hypoxia-induced iPS-BMECs cultured on the PET membrane and nEBM (Fig. 2e). Even though a remarkable change in the width of tight junction strands was not observed in the proposed BBB model, we confirmed the increased expression of ZO-1 in protein level by Western blot analysis (Fig. S5). This may partially explain the enhancement of the barrier integrity of the nEBM-based BBB model.

Additionally, the mRNA expression levels of the BBB markers were compared with the iPS-BMECs cultured on the nEBM against that

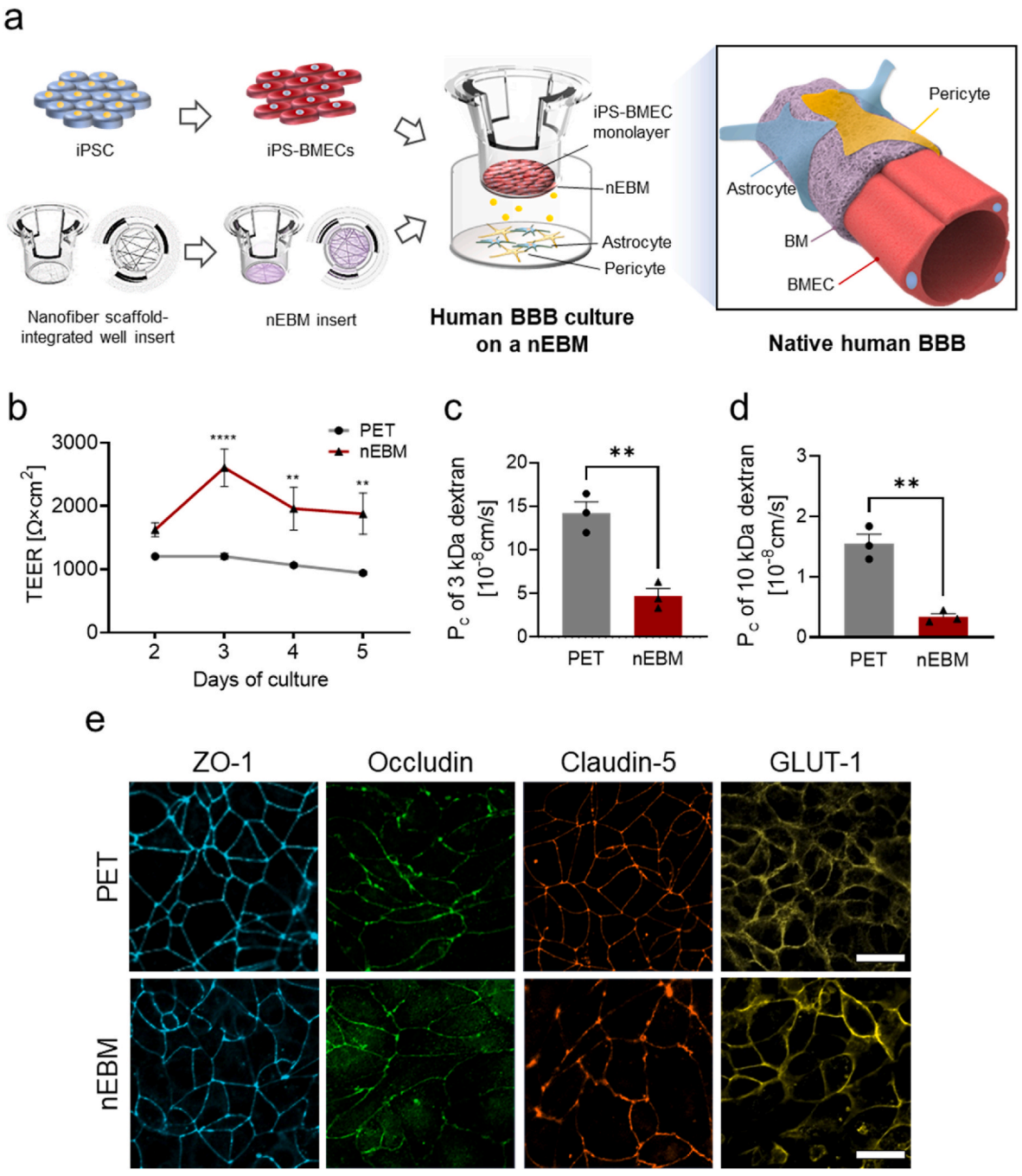

Fig. 2. Reconstruction of the human induced pluripotent stem cell (iPS)-derived BBB model on nEBM. (a) Schematic of a co-culture of hiPS-derived brain microvascular endothelial cells (iPS-BMECs), primary human astrocytes, and pericytes, using a nEBM insert system. The iPS-BMECs were cultured on the apical side of the nEBM, whereas the astrocytes and pericytes were cultured in the basal side in the lower chamber. (b) Measured transendothelial electric resistance (TEER) values of the BBB *in vitro* over the initial five days of culture on a PET membrane and nEBM. The results are presented as the mean ± s.e.m. (n = 3). For statistical analysis, two-way ANOVA was performed. (**P < 0.01; ****P < 0.0001). (c) Cellular permeability coefficient of 3 kDa dextran across BBB on PET membrane and nEBM. The results are presented as mean ± s.e.m. (n = 3). For statistical analysis, an unpaired *t*-test was performed. (**P < 0.01). (d) Cellular permeability coefficient of 10 kDa dextran across BBB on PET membrane and nEBM. The results are presented as the mean ± s.e.m. (n = 3). For statistical analysis, an unpaired *t*-test was performed. (**P < 0.01). (e) Immunofluorescence images of the BBB cultured on a PET membrane and nEBM, labeled with ZO-1, Occludin, Claudin-5, and GLUT-1. Scale bar = 20 μm.

cultured on the PET membrane (Fig. S6). No significant differences were observed in the mRNA levels of junctional protein genes including CDH5, CLD5, TJP1, OCLN, and PECAM1; solute carrier protein genes such as SLC1A1, SLC2A1, SLC7A5, SLC38A5, and P-glycoprotein (P-gp); and receptor protein genes such as ISNR, LRP1, and AGER and glycocalyx protein genes such as SDC1, SDC2, GPC1, HSPG2, and SDC4. Interestingly, iPS-BMECs on the nEBM exhibited significantly higher LAM mRNA expression compared to that developed on the PET membrane (Fig. S7), which indicates that nEBM better supports the secretion of laminin that is a key ECM glycoprotein of the BM. This verifies the successful application of the proposed culture method using a nEBM to create an *in vitro* human BBB without hampering the enhanced BBB attributes of hypoxia-enhanced iPS-BMECs [6].

2.3. Reorganization of F-actin enhancing junctional complexes of BBB on the nEBM through cellular mechano-response

The biophysical properties of BM are crucial, as they regulate gene expression in response to mechanical cues. Given the different biophysical characteristics of PET membrane and nEBM (Fig. 1), it was investigated if iPS-BMECs shows the distinct mechano-responses to those membranes. The formation of focal adhesion (FA) and organization of the cytoskeleton in iPS-BMECs cultured on the PET membrane and the nEBM were first examined, because the mechano-response of cells is generally initiated at the cell-substrate interface through integrin activation and clustering, forming FAs linked with actin filament bundles. To address the cell-ECM junction, iPS-BMECs were cultured in a low density and immune-stained for vinculin—a key mechanosensory protein in adhesion complex interconnecting actin filament to FA [35]. Fig. 3a shows a clear punctate structure of FAs in the iPS-BMECs developed on the PET membrane, whereas no clear punctate structures were observed on the nEBM. The FA size was significantly higher on the PET membrane (1.783 ± 0.25 μm^2) than on the nEBM (1.176 ± 0.16 μm^2) (Fig. 3c), indicating the formation of a greater number of mature FAs on the PET membrane. The influence of substrate properties on the FA size was in significant agreement with previous results, where the FA size were observed to increase in proportion to the Young's modulus of ECM [36–38]. This can be explained by the development of higher contractile stress on highly stiff ECMs, which eventually leads to large FA [36,37]. Since mature FA interacts with branched actin networks, the actin bundles of iPS-BMECs cultured on the PET membrane were observed to be more organized and thicker than those of iPS-BMECs on the nEBM. This is consistent with previous reports that ECM stiffness affects the actin cytoskeleton morphology [39]. These results demonstrate that iPS-BMECs can sense and respond to the biophysical features of nEBM, showing differential FA formations and F-actin organization compared to PET membrane.

The mechano-responses of iPS-BMECs on the nEBM were examined if they affect the junctional interactions between adjacent cells (Fig. 3b). It was hypothesized that a nEBM representing more similarity with the *in vivo* BM-like features compared to PET membrane would prompt the iPS-BMECs to develop stronger cell-cell adhesion. Vinculin is known to regulate the formation of junctions at both cell-cell and cell-ECM adhesions, by bridging the actin cytoskeleton to adherens junctions (AJs) and FAs. The position of vinculin (AJs or FAs) regulated by mechano-response of the cells governs the balance between cell-cell or cell-ECM adhesion, which results in the modulation of endothelial barrier function [24,40,41]. To observe the localization of vinculin at cell-cell junction and cell-ECM adhesion, vinculin and actin filament were immune-stained in the iPS-BMECs cultured in a high cell density. Fig. 3b shows the vinculins of iPS-BMECs on the PET membrane to be dominantly associated with cell-ECM adhesions indicated by the large-sized

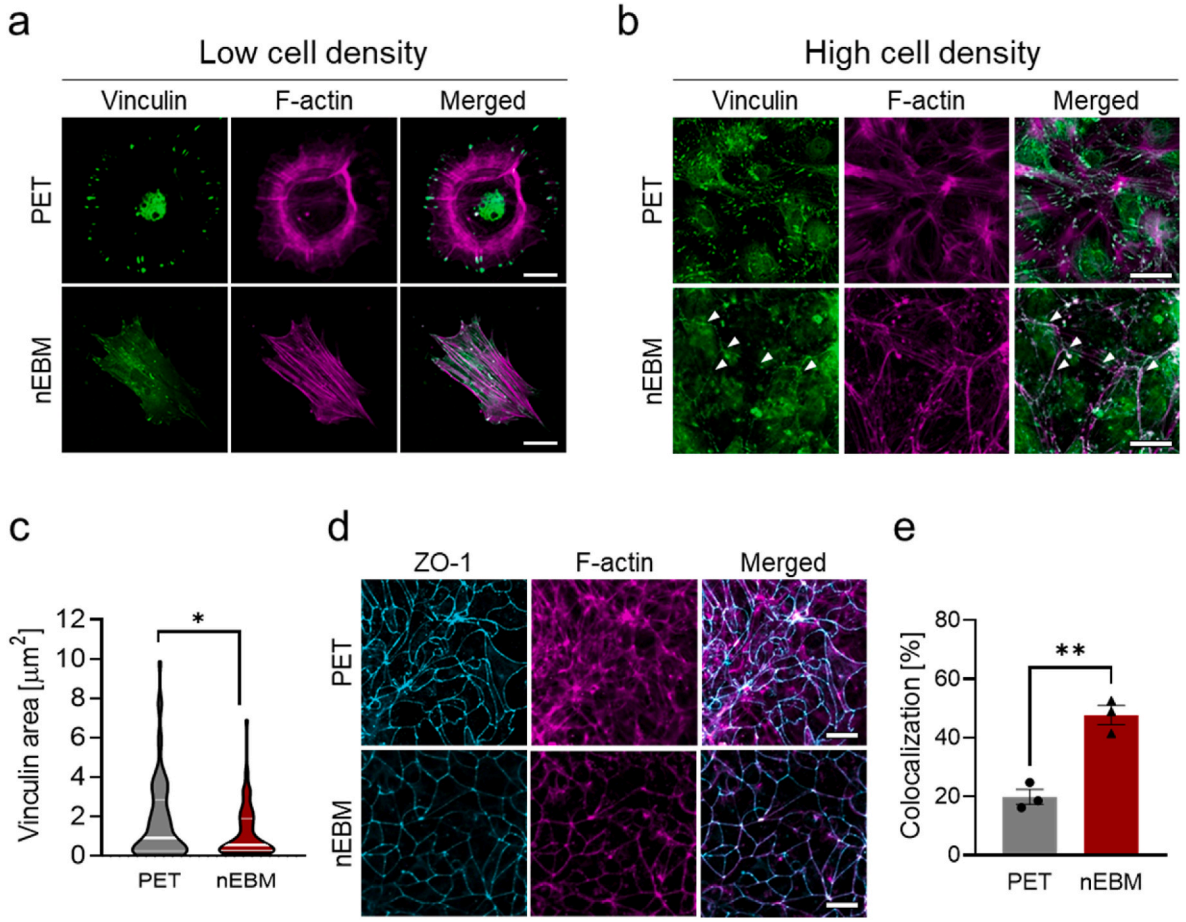

Fig. 3. Mechano-response of iPS-BMECs to the nEBM. (a) Immunofluorescence images of iPS-BMEC culture on each PET membrane and nEBM at low cell density, stained with vinculin (green) and F-actin (magenta). Scale bar = 20 μm. (b) High cell density. The white arrows indicate the vinculins localized along the cell border. Scale bar = 40 μm. (c) Area of vinculin in iPS-BMEC culture on the PET membrane and nEBM (n > 69). For statistical analysis, an unpaired *t*-test was performed (*P < 0.05). (d) Immunofluorescence images of BBB cultured on the PET membrane and nEBM, labeled with ZO-1 (turquoise) and F-actin (magenta), showing colocalized areas in white. Scale bar = 40 μm. (e) Colocalization efficiency of F-actin and ZO-1 analyzed through ImageJ. The results are presented as the mean ± s.e.m. (n = 3). For statistical analysis, an unpaired *t*-test was performed (**P < 0.01). (For interpretation of the references to colour in this figure legend, the reader is referred to the Web version of this article.)

mature FAs, with a trend similar to that in a low cell density (Fig. 3a). The actin-filaments were linked to the mature FAs, unlocalized at the cell-cell borders. On the contrary, vinculin was aligned along the cell-cell junctions together with actin-filaments on a nEBM, which shows the increased association of vinculins with cell-cell junctions rather than cell-ECM adhesions mediating the remodeling of actin-filament. This emphasizes that the nEBM, which offers relevant biophysical features of *in vivo* BM, empowered the balance of vinculin (mechanosensory protein) toward building the cell-cell junctions. These results are in agreement with a previous finding that an EC barrier enhancer (e.g., oxidized phospholipids) induces the vinculin association with the cell-cell junction anchored to the actin filament, while a barrier disruptive drug (thrombin) induces an association of vinculin with FA [40].

It is widely accepted that quiescent endothelial cells are characterized by a thick cortical actin ring, which reinforces the cell-cell junction, and by the absence of intracellular stress fibers that are associated with barrier dysfunction [42–44]. It indicates the importance of cytoskeleton distribution in the regulation of vascular endothelial barrier function. The arrangements of vinculin and actin-filament were demonstrated by the authors, previously, to be modulated by the nEBM. Based on this, the support provided by the nEBM for the formation of cortical actin enhancing the physical barrier function of the proposed BBB model was investigated. The immunofluorescence microscopic analysis confirmed the high enrichment of the stress fibers in the iPS-BMECs cultured on the PET membrane (Fig. 3d), whereas the iPS-BMECs on the nEBM formed a lower level of intracellular stress fibers and distinctive cortical actin fibers, indicated by the crosslinking of F-actin with ZO-1 (Fig. 3d). The colocalization efficiency of F-actin and ZO-1 in the nEBM was 47.7%, which was 2.4 times as much as that in the PET membrane, confirming the enhancement of the assembly of cortical actin by the nEBM, which is necessary for the establishment of intercellular adhesion and the maintenance of endothelial barrier (Fig. 3d). Thus, the recapitulation of the physical barrier function of BBB on the nEBM can be explained by two factors: the localization of vinculin, derived from the formation of focal adhesion, and the formation of cortical actin ring colocalized with junctional proteins, induced by the mechano-stimuli from the soft membrane.

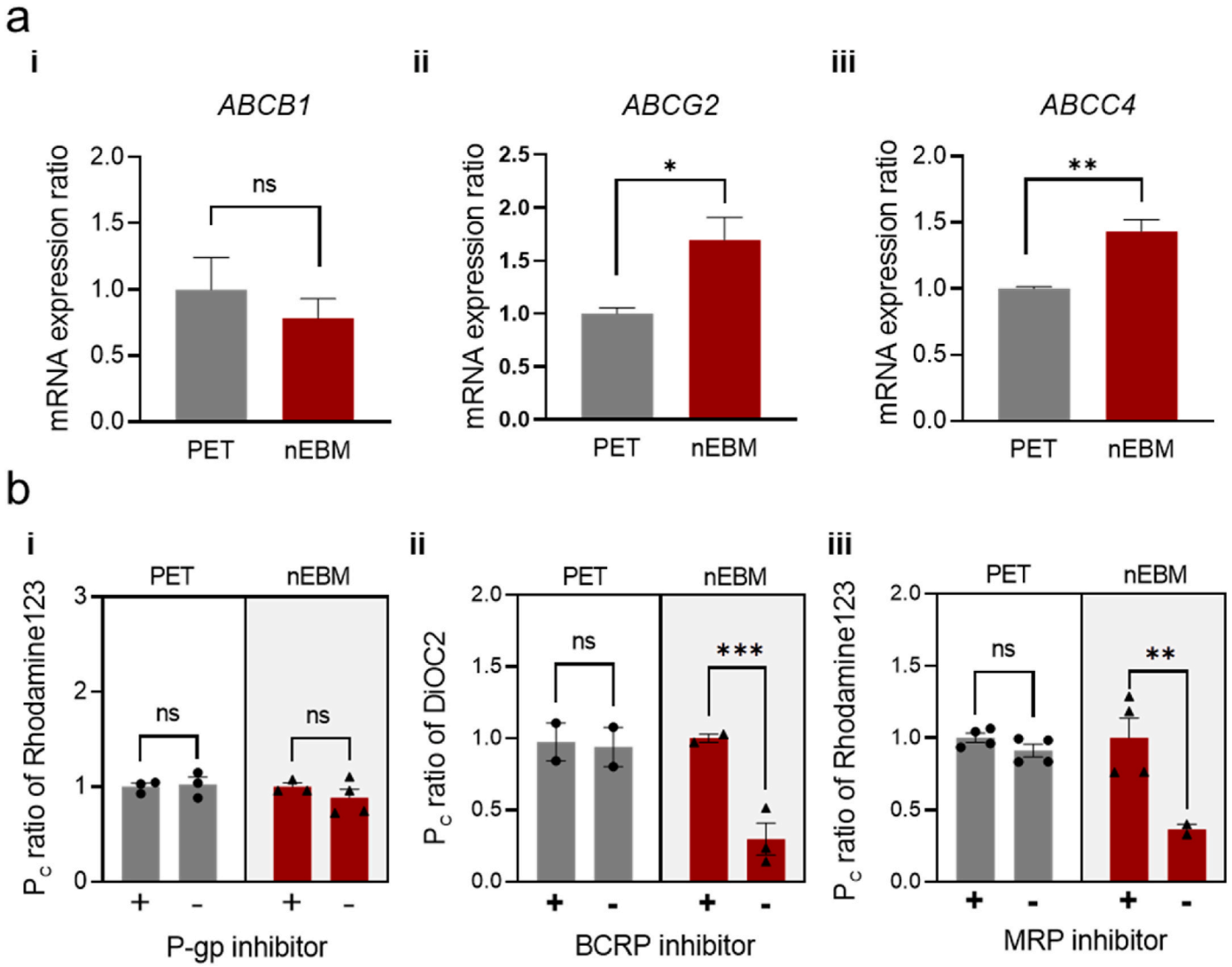

Fig. 4. Enhanced metabolic barrier function of BBB on the nEBM. (a) Quantitative RT-PCR of the BBB on the PET membrane and nEBM. Relative mRNA expression of the genes encoding efflux pump proteins was analyzed (n = 3). The results are presented as mean ± s.e.m. For statistical analysis, an unpaired *t*-test was performed (*P < 0.05; **P < 0.01). (b) BBB efflux pump substrate measured through rhodamine123 as a substrate of P-gp and MRP1; DiOC2 as a substrate of BCRP with or without the addition of efflux transporter inhibitors (verapamil for P-gp, MK 571 for MRPs, and Ko143 for BCRP). The results are presented as mean ± s.e.m. For statistical analysis, a two-way ANOVA was performed (**P < 0.01; ***P < 0.001).

2.4. Enhanced metabolic barrier function of BBB on the nEBM

One of the most important functions of the BBB is the protection of brain from xenobiotics and potentially poisonous metabolites [45]. The detection of drug-related ABC efflux transporters such as P-glycoprotein (P-gp), breast cancer resistance protein (BCRP), and multidrug resistance protein (MRP), are the primary features of the BBB, localized on the luminal side of the membrane. They recognize various substrates and pump them back to the bloodstream [46,47]. The activities of efflux pump proteins are therefore important for the prediction of the *in vivo* BBB permeability properties of drug candidates, when constructing *in vitro* BBB model. However, some published studies on the *in vitro* BBB models constituted from iPS-derived BMECs have failed to develop the level of efflux pump protein depending on the differentiation method, which results in the low predictability of the CNS drug permeability through the *in vivo* BBB [48–51]. Therefore, efforts have been taken to enhance the efflux proteins, such as providing shear stress and treating chemicals to enhance the metabolic barrier functions [6,52].

The induced enhancement of metabolic barrier function of BBB by the nEBM with microenvironments similar to *in vivo* BM was investigated, by observing the expression levels of genes that encode P-gp (ABCB1), BCRP (ABCG2), and MRP4 (ABCC4), and by comparatively analyzing the activities of the BBB efflux transport proteins with respect to the BBB model constructed on the PET membrane. No difference was observed for the ABCB1 expression (Fig. 4a–i) between the two groups, which agrees with a previous finding that the substrate stiffness does not change ABCB1 expression in iPS-BMECs [24]. On the other hand, small but significant increases in the expression levels of ABCG2 (Fig. 4a–ii) and ABCC4 (Fig. 4a–iii) were identified in the iPS-BMECs cultured on the nEBM against that on the PET membrane. Subsequent tests were performed on the proposed nEBM-based *in vitro* BBB model to verify its recapitulation of functional metabolic barriers. The BBB models were pretreated with inhibitors including verapamil, Ko143, and MK461, which target P-gp, BCRP, and MRP4, respectively, and the BBB penetration of efflux pump substrates, rhodamine123, and DiOC2, were monitored. The treatment of P-gp inhibitor was observed to produce no influence on the transport of rhodamine123 through BBB, implying that P-gp was not functionally active in both BBB models. Given that rhodamine 123 is also a substrate of MRP4, we confirmed this result independently in the presence of both P-gp and MRP4 inhibitors to rule out the effect of MRP activity (Fig. S8). This agrees with the observations in previous studies, which revealed the level of P-gp activity to be low in static BBB culture conditions [6,52]. Furthermore, the inhibition of BCRP (Fig. 4b–ii) and MRP4 (Fig. 4b–iii) resulted in the significant increase of the apical to basal transport of substrates, by 3.4 and 2.7 times respectively, in the BBB model developed on the nEBM. On the other hand, when conducting similar studies with BBB model cultured on the PET membrane, we observed no change in the influx of substrate. The BCRP and MRP4 proteins are localized at the apical membrane of brain endothelial cells, where it mediates unidirectional transport of substrates to the luminal side of the BBB [53]. To validate the luminal expression of those proteins in iPS-BMECs on the nEBM, we monitored the basolateral-to-apical transport of substrates in the presence of efflux pump inhibitors. On the contrary to the apical-to-basal permeability of BMECs (Fig. 4b–ii and iii), the basolateral-to-apical transport of substrates was not changed (Fig. S9). These results demonstrate that the nEBM enabled the recapitulation of the important efflux transport functions of the human BBB, mediated by BCRP and MRP4, in addition to the physical barrier function that is highly relevant to drug development processes.

2.5. Use of in vitro human BBB on the nEBM as an ischemic stroke model

One of the pathophysiological features of ischemic stroke, which accounts for 87% of all strokes, is the disruption of the BBB, which significantly contributes to the development of brain injury and subsequent neurological impairment [54,55]. When an ischemic stroke occurs, blood flow to the brain is interrupted resulting in decreased oxygen delivery and nutritional supply to the affected part of the brain, followed by a rapid return of blood flow to the brain, which results in the loss of BBB integrity with tight junction alterations, increased vesicular trafficking, leukocyte infiltration, and further inflammatory responses [56]. To understand the molecular mechanism of BBB disruption in ischemic stroke and to develop therapeutic strategies for stroke, *in vitro* ischemic stroke BBB models have been developed. However, their poor physiological relevance limited the reliability of the analysis of ischemic BBB injury, consequently, testing for stroke injury treatment. Therefore, the proposed BBB system was studied to verify its application for modeling ischemic stroke, by mimicking hypoglycemic and hypoxic environments under ischemia followed by reoxygenation. The *in vitro* BBB was exposed to acute oxygen-glucose deprivation (OGD) for 8 h, and normal oxygen and high glucose levels for additional 16 h [57], and cellular responses were investigated. Furthermore, the effectiveness of metformin, which has been demonstrated to improve functional recovery in ischemic animal model, was examined with the proposed model (Fig. 5a) [58,59].

The degree of diminished BBB integrity was evaluated by measuring the TEER at different time points of OGD and reperfusion (Fig. 5b). The analysis of TEER at 8 h after OGD revealed no significant difference between the normal and ischemic stroke model. However, a dramatic decrease in TEER was detected at 8 h after reperfusion, which indicates that the proposed model successfully reflected the responses observed in ischemic stroke patients when drugs involved in the breakdown of blood clots are administered [57,60]. Consistent with *in vivo* observation, exposure to metformin resulted in a relatively low decrease in barrier integrity after reoxygenation, which recovered to normal levels within 8 h. Additionally, the loss of barrier integrity, observed in the ischemic stroke model, was accompanied by a damage in junctional complexes. Fig. 5c shows that the confocal immunofluorescence analysis of the ischemic stroke model revealed the partial loss of ZO-1 at the region of cell-cell contact, demonstrating the tight junction disruption, whereas the tight junctions were confirmed to be intact under treatment with metformin. Moreover, both the ischemic stroke models, in the presence and absence of metformin, exhibited a higher GLUT-1 expression than the normal BBB model (Fig. 5d). This agrees with a previous finding that the stroke stimuli induce the upregulation of GLUT-1 expression from the BBB, because of the considerably high requirement of glucose metabolism from brain cells to confront the severe energy depletion [61–63].

Subsequently, the human BBB system was investigated for its recapitulation of the transendothelial immune cell infiltration and migration under an acute ischemic stroke. After exposure to OGD and reoxygenation, the human BBB reconstructed on the nEBM was co-cultured with macrophages (RAW 264.7) stained with CellTracker green dye from the apical side, and interactions of the macrophages with iPS-BMECs were monitored under a confocal microscope. Owing to the transparency of the ultra-thin nEBM enabling clear visualization of the cell movement, the macrophages were observed to be crawling and migrating across the iPS-BMEC monolayer. The time-lapse image sequences identified multiple macrophages stained with green dye at the basal side of the BM (from t = 0–17 min) under the ischemic stroke conditions. This mimicked the peripheral immune cells that infiltrate the ischemic brain across the BBB observed *in vivo* (Fig. 5e). Furthermore, macrophages were observed at the basal side of BM (t = 8 min), while they vanished from the apical side of iPS-BMEC monolayer owing to transmigration across the BBB (Fig. 5e, Movie S1). A confocal microscopic image from the side view revealed the macrophages labeled with a green dye at the basal side of nEBM, owing to their transmigration across the BBB under the conditions similar to ischemic stroke (Fig. 5f). In contrast, the normal BBB on the nEBM did not allow the transmigration of macrophages owing to its strong barrier integrity. Together, these results confirmed that the nEBM based BBB model could recapitulate the

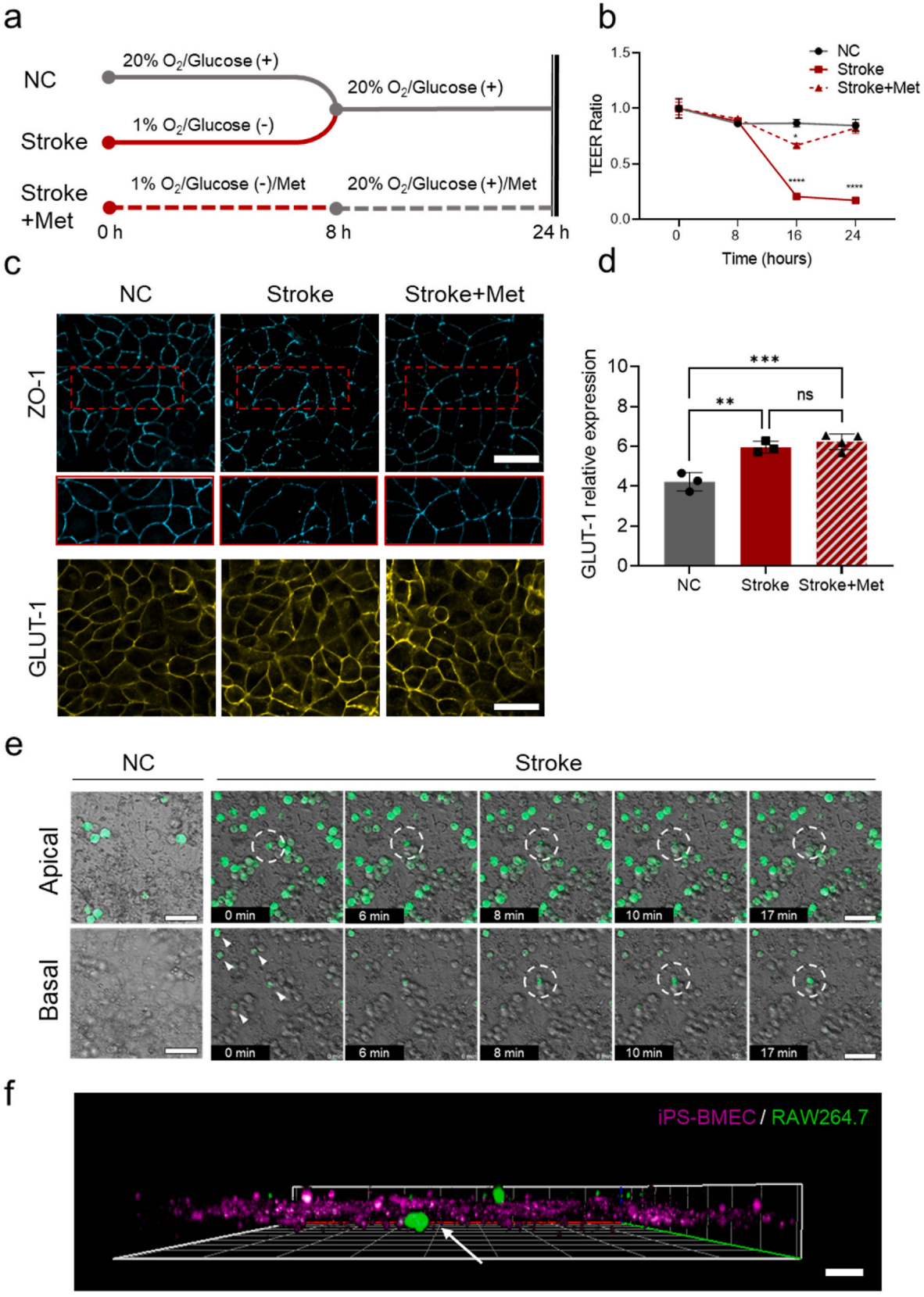

(caption on next page)

Fig. 5. Use of *in vitro* human BBB on the nEBM for ischemic/stroke model. (a) Timeline for establishing stroke model: For normal control (NC), the cells were incubated under normoxic conditions (20% O_2, 5% CO_2) with glucose for 24 h. For stroke with and without metformin (Met), the cells were incubated under hypoxic conditions (1% O_2, 5% CO_2) in the absence of glucose with or without metformin for 8 h, followed by reoxygenation for 16 h under normoxic conditions with glucose. (b) Change in TEER values at regular time intervals (8, 16, and 24 h). The TEER measurements were normalized to the TEER at 0 h (n = 2 for each condition). For statistical analysis, two-way ANOVA was performed (*P < 0.05; ****P < 0.0001). (c) Immunostaining images of iPS-BMECs labeled with ZO-1 and GLUT-1. Scale bar = 20 μm. (d) The relative expression level of GLUT-1 analyzed by ImageJ; the data are presented as mean ± SED. For statistical analysis, one-way ANOVA was performed (**P < 0.01; ***P < 0.001). (e) Representative time-lapse images showing macrophage transendothelial migration from apical to basal side of nEBM under normal and ischemic stroke-like conditions. The white arrows indicate Raw264.7 cells in transmigration; white triangles at 0 min indicate transmigrated Raw264.7 cells detected at the basal side of nEBM. Elapsed times are shown above each panel. Scale bar = 40 μm. (f) Representative 3D images showing immunofluorescent staining of iPS-BMEC layer (ZO-1; red) for indicating brain endothelium and CellTracker green-stained Raw264.7 (Green). The white arrow indicates Raw 267.7 cells that transmigrated across the brain endothelium and nEBM. Scale bar = 20 μm. (For interpretation of the references to colour in this figure legend, the reader is referred to the Web version of this article.)

cellular responses under ischemic stroke conditions, including a loss of barrier function and upregulation of GLUT-1. It enabled an effectively visualized study of immune cell transmigration through a nEBM exhibiting high permeability similar to *in vivo* BM.

Supplementary data related to this article can be found at https://doi.org/10.1016/j.biomaterials.2022.121983.

3. Discussion

Since the biophysical/chemical properties of BM dominate the physiological functions of neighboring cells, the development of engineered BMs has emerged as a promising way of enhancing cellular functions of tissue/organ models [22]. *In vitro* human BBB models have evolved rapidly owing to recent technological advances including stem cell engineering [8], biomaterials [64], and microfluidics [6]. However, the importance of BMs where cell phenotypes are regulated has been neglected. This is because of the difficulty in recapitulating the BM features from both biophysical and biochemical perspectives, and the difficulty in integrating it into a cell-based assay [22]. Therefore, the development of compartmentalized BBB models based on Transwell or microfluidic systems and commercially available porous polymeric membranes have widely been used, despite their suboptimal properties.

In this study, a novel approach to recapitulate the specialized barrier functions of human BBB was demonstrated at a physiological level with nEBM, which is an *in vivo* BM-mimicking ECM hydrogel membrane. The nEBM was composed of collagen I/collagen IV/fibronectin hydrogel reinforced by an ultra-thin and sparse nanofiber scaffold, which could be easily incorporated into a Transwell insert frame through a novel thermal bonding method. Collagen IV and fibronectin have been routinely used to culture iPS-BMEC based on the biological consideration that collagen IV makes up about 50% of all BM components and fibronectin is a highly enriched non-collagenous glycoprotein in BM [8,65,66]. On the other hand, collagen I gel underlying the mixture of collagen IV and fibronectin is not the main component of BM ECM; however, it was used to provide stable structural support to iPS-BMEC and allow for ease of controlling mechanical property of substrate in many previous BBB models [65]. In nEBM, the nanofiber scaffold coated with collagen I gel functioned as a structural element, and above this, collagen IV/fibronectin provided biochemical support for iPS-BMECs. It exhibited a stiffness similar to that of *in vivo* (approximately 500 kPa), a low thickness (5 μm), and high permeability, compared to PET membrane. The nEBM-based human BBB system exhibited highly enhanced barrier functions at a physiological level, achieved by the mechano-response of iPS-BMEC to physiological stiffness. The mechanical stimuli of the nEBM were observed to induce the relocalization of vinculin and the formation of actin cortical ring, which resulted in the formation of a stronger cell-cell junction. Further, the improvement of metabolic barrier activity was examined together with the upregulation of gene expressions that encode efflux pump proteins, which is critical for reliably studying drug transportation across the BBB. To the best of the authors' knowledge, this is the first study to reveal that engineered BM possessing both *in vivo* BM-like biochemical and mechanical characteristics can facilitate the recreation of physiological barrier functions of the BBB. For further mechanomic understanding of cell behaviors on the nEBM, in-depth investigation on mechanotransduction of brain endothelial cells using transcriptomic and proteomics analysis is required. This will be important to guide future research on developing advanced BM engineering for sophisticated regulation of barrier function of BBB *in vitro*.

Furthermore, the human BBB system was demonstrated to be used in the modeling of ischemic stroke, reproducing the dynamic changes of BBB, including the loss of barrier integrity, GLUT-1 upregulation, and immune cell infiltration observed in patients. The nEBM was observed to facilitate the transmigration of immune cells across the BBB through the hydrogel space between highly sparse nanofibers without hindrance, in contrast to that observed in polymeric membranes with low porosity or small sized pores. In addition, the high optical transparency of nEBM allowed the accurate microscopic analysis of immune cell transmigration. Growing evidence suggests that ischemic stroke activates the peripheral immune system, which leads to the influx of immune cells into the ischemic infarct, affecting both the early disruption and the later repair of the BBB [67]. The proposed BBB system is believed to provide a highly accurate model for the assessment of cell transmigration under ischemic stroke conditions and for studying the related intercellular mechanism.

The nEBM was considerably advantageous in BBB modeling over previously developed electrospun nanofiber-based membranes [25,68,69]. Qi et al. established an iPS-BBB model based on Matrigel-coated poly (lactic-co-glycolic) acid (PLGA) nanofibers. Though a Young's modulus of the membrane (50 MPa) is far smaller compared to the PET membrane (2 GPa), it is still over 100 folds higher than that of the BM owing to the high density of the fiber [26]. Bischel et al. developed a membrane based on gelatin nanofibers having a Young's modulus as low as 5 MPa. The barrier integrity of the BMECs was enhanced on the soft gelatin membrane compared to the stiff PET membrane [25] despite the lack of BM-like biochemical cues, however, it was not relevant to *in vivo* BBB level. The proposed method in this study enabled the engineering of BM with more similar features to *in vivo*, compared to previous studies, owing to the thin and loosely fabricated nanofiber scaffold and *in vivo* relevant hydrogel components, which resulted in the recapitulation of BBB functions at a physiological level. To our knowledge, this is the first demonstration of a nanofiber-based membrane capable of enhancing the barrier functions of BMECs by eliciting cellular mechanoresponses. This reveals how designing basement membrane with faithful biomimetic features can improve the potential functionality of BBB *in vitro*.

In addition to the biophysical features of the substrate, the biochemical cues derived from ECM components can highly influence the barrier properties of BBB platform [70–73]. The importance of matrix composition in barrier function of iPS-derived BBB model was demonstrated in a previous study where the addition of collagen IV, fibronectin, and laminin promoted cell adhesion, spreading, and formation of junctional complexes of iPS-BMECs [65]. Accumulating evidence shows that laminin, which is the most abundant non-collagenous glycoprotein in BM, plays key roles in vascular integrity regulation by interaction with integrin α1β1 and α6β1 [74–76]. Although laminin was not incorporated in nEBM, we confirmed the upregulated laminin expression in iPS-BMECs when cultured on the nEBM compared to the

PET membrane. We assume that facilitated chemical communications of BMECs with astrocytes and pericytes through a highly permeable nEBM could expedite the laminin secretion of iPS-BMECs [77]. Additionally, it will be interesting to see whether an extra-coating of laminin or laminin-enriched Matrigel on the nEBM would enhance the barrier integrity of iPS-BMECs. In particular, the use of a specific type of laminin that is more enriched in BBB such as laminin-511 [74] may be a useful strategy for improving the BBB attributes of iPS-BMECs.

4. Conclusion

A multicellular human BBB model created on the nEBM, offering *in vivo* BM-like biophysical/chemical environments, exhibited highly enhanced barrier functionalities compared to previous BBB models. We discovered that the physical barrier function of BBB was enhanced owing to the regulated cellular mechano-response by the nEBM, resulting in the formation of stronger junctional complexes. The nEBM also enabled the recapitulation of the functional activity of efflux pumps (BCRP and MRP4), thus verifying its utility for the development of drugs that selectively cross the BBB. Additionally, the pathological process, therapeutic response, and immune cell transmigration under the conditions of ischemic stroke were successfully reproduced using the enhanced BBB model. Therefore, the proposed nEBM based human BBB system can offer a robust *in vitro* platform for translational research in drug discovery and development of therapeutic strategies for treatment of brain diseases. This study strongly suggests a new opportunity for future research on meliorating engineered BM to develop an advanced model of human BBB. The current study can offer a foundation for future studies on improving the biophysical/chemical properties of nEBM, by modifying the electrospinning materials, process, and alignments, or by using more relevant ECM proteins such as brain decellularized ECM hydrogel and Matrigel.

5. Experimental sections

Preparation of electrospun nanofiber scaffold-integrated well insert. The SF extracted from a silk cocoon (Jayeoncho, South Korea) was prepared using the same process described in the previous study [78,79]. A mixture solution of the extracted SF and PCL (average Mn = 80,000; Sigma-Aldrich, USA) was prepared by dissolving both SF and PCL in 1,1,1,3,3,3-hexafluoro-2-propanol (Sigma-Aldrich, USA) with an SF/PCL ratio of 1:1 (w/w) to have a final concentration of 5% (w/v). The SF/PCL solution was loaded in a gastight glass syringe (Hamilton, USA) with a 23-gage metal needle (NanoNC, South Korea). The SF/PCL solution loaded in the glass syringe was ejected at a constant flow rate of 1 mL h^{-1} with a syringe pump in the electrospinning machine (NanoNC, South Korea). A high voltage of 15 kV was applied between the metal needle and a hollow-cylindrical aluminum collector placed 14 cm below the metal needle at a relative humidity of 50–60% and temperature of 20–25 °C. The electrospinning process was performed for 1–3 min to fabricate a free-standing, sparse SF/PCL nanofiber scaffold for each well insert, and 10 min for a high-density nanofiber scaffold.

A well insert with no membrane was custom-designed to be fitted with the 24-well plate and produced using an injection molding machine (SE50D; Sumitomo, Japan) with polystyrene (PS) pellet (DowChem, USA). The PS well insert preheated at 105 °C on a hot plate (NanoNC, South Korea) for 10 min and the free-standing electrospun SF/PCL nanofiber scaffold was transferred on the bottom opening of well insert and pressed to be thermally bonded.

Fabrication of nEBM. A nanofiber scaffold-integrated well insert was immersed in 70% EtOH and washed with Dulbecco's phosphate-buffered saline (DPBS; Welgene, South Korea) twice just before coating. To form an ultra-thin layer of ECM hydrogel throughout the nanofiber scaffold, 0.2 mg mL^{-1} rat tail type I collagen (Corning, USA) in DPBS was treated to the apical and basal sides of membrane and incubated for 1 h at 37 °C. Additionally, a layer of BM ECM molecules was created on a type I collagen hydrogel by coating with a mixture of 0.4 mg mL^{-1} human placenta-derived type IV collagen (Sigma-Aldrich, USA) and 0.1 mg mL^{-1} fibronectin (Sigma-Aldrich, USA) in DPBS on an apical side of a type I collagen on the nanofiber scaffold at 37 °C overnight.

Thickness measurement of nEBM. The fabricated nEBM was embedded carefully into the degassed uncured polydimethylsiloxane (PDMS; 10:1, w/w) and cured at 55 °C for 24 h. The nEBM embedded in the PDMS was cut near the centreline to show the membrane cross-section with a razor blade. The cross-section images of the nEBM were obtained using a phase-contrast microscope (Carl Zeiss, Germany), and the thickness was measured after converting to the optical image to a 16-bit image using the ImageJ (NIH, USA) software. As a control group, the thickness of commercial PET membrane was also measured with the same procedure.

Stiffness measurement of nEBM. Stiffness of the nEBM was assessed using a custom-made instrument which is designed to measure the membrane deformation after loading a metal ball on the center of the membrane with a similar concept to the instrument introduced in previous work [80]. The center displacement of the membrane (δ) was measured using a camera (NIKON, Japan) and a Young's modulus (E) was calculated from the following equation (1), where w is the weight of the ball, h is the membrane thickness and R is the radius of the ball.

$$\frac{6w}{EhR} = 0.075\left(\frac{\delta}{R}\right)^2 + 0.78\left(\frac{\delta}{R}\right) \quad (1)$$

Scanning electron microscopy analysis. The nEBM was fixed with 2.5% (w/v) glutaraldehyde (Sigma-Aldrich, USA) diluted in deionized (DI) water for 10 min. After rinsing with DI water gently, the nEBM was dehydrated in a graded ethanol series (30%, 50%, 70%, 90%, and 100% in DI water, v/v). The nEBM was dried at 4 °C overnight and sputter-coated with platinum at an electric current of 15 mA for 120 s. The microstructure of the surface of nEBM was examined using a field-emission SEM (SU6600; Hitachi, Japan).

Human iPS-BMECs differentiation. The human induced pluripotent stem cell line (IMR90-4) was purchased from WiCell Research Institute and maintained on Matrigel (Corning, USA) using TeSR™-E8™ (Stemcell Technologies, Canada) according to WiCell Feeder Independent Pluripotent Stem Cell Protocols provided by the WiCell Research Institute (http://www.wicell.org). Human induced pluripotent stem cell (iPSC) derived brain microvascular endothelial cells (iPS-BMECs) were differentiated from iPSCs as previously described with minor modifications [6]. To generate the iPS-BMECs, maintained iPSCs were singularized using Accutase (Merck, USA). The harvested cells were counted and seeded at a density of 1.7×10^4 cells per well on a Matrigel coated 6-well plate in TeSR™-E8™ supplemented with 10 μM ROCK inhibitor (Y-27632; Tocris Bioscience, UK). The iPSCs were expanded until the cell density reaches at 2.5×10^5 cells per well. To initiate differentiation at D0, the medium was switched to an unconditioned medium (UM): 78.5% DMEM/F12 (Thermo Fisher Scientific, USA), 20% Knockout™ Serum Replacement (Thermo Fisher Scientific, USA), 1% Non-Essential Amino Acids (100 ×) (Thermo Fisher Scientific, USA), 0.5% GlutaMAX™ supplement (Thermo Fisher Scientific), and 0.007% β-mercaptoethanol (Thermo Fisher Scientific, USA). After 24 h, the culture medium was changed with fresh UM every day for another five days. The endothelial cells were selectively expanded for two days by switching to endothelial cell medium (EC) composed of Human Endothelial SFM (Thermo Fisher Scientific, USA) supplemented with 1% human serum (Sigma-Aldrich, USA), 20 ng mL^{-1} human basic fibroblast growth factor (bFGF; PeproTech, USA), and 10 μM retinoic acid (Sigma-Aldrich, USA) at D6. On D8, differentiated cells were dissociated with Accutase and plated onto ECM-coated 0.4 μm PET Transwell inserts (Corning, USA) or nEBM inserts to reconstruct the BBB. In order to improve the BBB attributes of iPS-BMECs, cells were exposed to low oxygen tension (5% O_2, 5% CO2) during differentiation from D0 to D9 using a hypoxic chamber (Galaxy® 48 R; Eppendorf) as previously reported [6].

ECM Coating on a PET membrane. A PET membrane (0.4 μm pore size) (Corning, USA) was coated with a type I collagen and subsequently with a mixture of type IV collagen and fibronectin, with the same process of coating for nEBM fabrication. In detail, 0.2 mg mL^{-1} rat tail type I collagen (Corning, USA) in DPBS was treated to the apical and basal sides of PET membrane and incubated for 1 h at 37 °C. Then, a mixture of 0.4 mg mL^{-1} human placenta-derived type IV collagen (Sigma-Aldrich, USA) and 0.1 mg mL^{-1} fibronectin (Sigma-Aldrich, USA) in DPBS was treated on an apical side of the PET membrane at 37 °C overnight.

Reconstruction of BBB in a PET Transwell and nEBM insert. Human primary astrocytes (Cat#1800; ScienCell, USA) and human primary pericytes (Cat#1200; ScienCell, USA) were purchased and maintained in Astrocyte Medium (ScienCell, USA) and Pericyte Medium (ScienCell, USA) respectively. A mixture of astrocytes (1.16×10^4 cells per well) and pericytes (0.58×10^4 cells per well) was seeded on a 24 well-plate at 1 d before seeding the iPS-BMECs. On D8, the iPS-BMECs differentiated from iPSCs were dissociated and plated in 200 μL EC medium onto a PET membrane insert at a density of 16.5×10^5 cells per mL. To culture the iPS-BMECs on a nEBM insert, iPS-BMECs were plated in a smaller volume of EC medium (50 μL) at a higher density (66×10^5 cells per mL) to prevent the damage in a soft membrane owing to the hydrostatic pressure. The PET Transwell and nEBM inserts plated with iPS-BMECs were placed to the 24 well-plates where astrocytes and pericytes were cultured. At 6 h after seeding iPS-BMECs, EC medium was carefully added onto the apical side of insert. After 24 h, the medium was switched to EC medium deprived of human bFGF and Retinoic acid and changed daily for maintenance of BBB culture. The TEER ($\Omega \times cm^2$) measurement was performed daily to assess the barrier integrity of the BBB using EVOM2 (World Precision Instruments., USA). The following experiments were conducted on the third day of cell seeding on the inserts.

To monitor the TEER values of HUVEC monolayer on a PET and nEBM, HUVECs (Lonza, Switzerland) were grown in Endothelial Cell Basal Medium supplemented with EGM-2 MV Bulletkits in T75 flask. When it reaches 80% confluency, HUVECs were detached and seeded on a PET transwell and nEBM at 3×10^4 cells per insert. HUVECs were cultured additional two days to reach confluency and TEER values were measured every day.

Permeability assay. Apparent permeability (P_{app}) of the barrier was calculated by analyzing the amount of the dextran tracer penetrated across the membrane. The PET membrane and nEBM were apically treated with 100 μg mL^{-1} Dextran, Cascade Blue (3 kDa and 10 kDa) (Invitrogen, USA) with the presence or absence of cells and incubated shaking for 2 h at 37 °C. The basal effluents were collected and the concentration of the dextran tracer was determined by using a microplate reader (SynergeNeo2; Biotek, USA). The following equation (2) [81] was used to calculate the P_{app}.

$$P_{app} = \frac{C_x}{C_0 \times t(s) \times A(cm^2)} \times V(cm^3) \quad (2)$$

C_0 is a concentration of dextran tracer apically applied and C_x is a concentration of a dextran tracer in the basal effluent at time t. A is the area of the membrane, and V is the volume of the medium in the basal chamber.

Then, the permeability of cell P_c on the membranes were calcuated as follows.

$$\frac{1}{P_c} = \frac{1}{P_{app}} - \frac{1}{P_m}$$

where P_{app} is the apparent permeability coefficient for combined permeability of a cell layer and a membrane and P_m is the permeability coefficient of the only membranes without cells [82,83].

Immunofluorescent imaging. The iPS-BMECs were fixed with 4% paraformaldehyde (Biosesang, South Korea) for 15 min and permeabilized with 0.1% of Triton- X100 (Sigma-Aldrich, USA) in DPBS for 10 min at room temperature (RT). Next, the samples were blocked with 10% goat serum in 0.1% of Triton-X100 for 1 h at RT, and then the adequate concentration of primary antibodies in 10% goat serum (Thermo Fisher Scientific, USA) in DPBS were treated overnight at 4 °C. The primary antibodies used in this study are listed in Table S2. After washing the samples with DPBS three times, fluorescent-dye conjugated secondary antibodies were treated for 1 h at RT. Nuclei and F-actin were counterstained with 1 μg mL^{-1} of 4′,6-diamidino-2-phenylindole (DAPI; Sigma-Aldrich, USA) and 1:400 dilution of Phalloidin (Invitrogen, USA). After the washing process, a mounting medium (Leica, Germany) was dropped on both the cells and the bottom of the insert to integrate with the cover glass for imaging. Fluorescence images of the cells were obtained using a confocal microscope (LSM980; Zeiss, Germany).

Real-time polymerase chain reaction (PCR). Total RNA of the iPS-BMECs was extracted using a AccuPrep® Universal RNA Extraction Kit (Bioneer, South Korea) and reverse-transcribed into cDNA using AccuPower® RT PreMix & Master Mix (Bioneer, South Korea) in a thermal cycler (T100 Thermal Cycler; Bio-Rad, USA). The real-time PCR was carried out using SYBR® Green Realtime PCR Master Mix (TOYOBO, Japan) on a CFX Connect Real-Time PCR Detection System (Bio-Rad, USA). Table S3 lists the primer sequences used for real-time PCR.

Metabolic barrier function assay. P-gp, BCRP, and MRP functionalities were assessed using Rhodamine 123 (Sigma-Aldrich, USA) and DiOC2 (3,3′-Diethyloxacarbocyanine Iodide; TCI, Japan). The BBB on the PET membrane and nEBM were pretreated with or without 50 μM Verapamil (P-gp inhibitor; Sigma-Aldrich, USA), 1 μM Ko143 (BCRP inhibitor; Sigma-Aldrich, USA), and 10 μM MK571 (MRP inhibitor; Sigma-Aldrich, USA) for 30 min at 37 °C. The cells were apically treated with 2 μM Rhodamine 123 and 2 μM DiOC2 and incubated for 1 h on a shaker. The basal effluent (100 μL) was collected and the concentration of substrates was determined by measuring the fluorescence intensity at 485/530 nm (Rhodamine 123) and 482/497 nm (DiOC2) using a microplate reader (SynergeNeo2; Biotek). The TEER value was also measured before and after the assay to confirm the barrier integrity of the BBB models.

Establishment of stroke injury model. For stroke experiment, DMEM without glucose (Thermo Fisher Scientific, USA) was used instead of EC medium. For normal condition (negative control), the BBB developed on nEBM was incubated in DMEM without glucose supplemented with 5.5 mM of D-glucose (Sigma-Aldrich, USA) in a 37 °C incubator (22% O_2 and 5% CO_2). For the stroke model, the BBB developed on nEBM was incubated in a hypoxia chamber (1% O_2 and 5% CO_2; Eppendorf, Germany) for 8 h in DMEM without glucose. At 8 h, oxygen and glucose were supplied by adding concentrated glucose solution (1 M) to the apical and basal chamber and placed in a 37 °C incubator (22% O_2 and 5% CO_2) for the indicated time. For the stroke/met group, 10 μM of metformin (Sigma-Aldrich, USA) was added in the medium at 0 h. Because TEER is temperature sensitive, BBB cultures were placed at room temperature for 15 min until thermal equilibrium was established before measurement.

Live imaging of macrophage transmigration. Raw264.7 cells were purchased from Korean Cell Line Bank (KCLB; South Korea) and cultured in Dulbecco's modified Eagle's Media (DMEM; Welgene, South Korea) supplemented with 10% fetal bovine serum (FBS; Merck, USA) and 1% Penicillin-Streptomycin (P/S; Thermo Fisher Scientific, USA) solution according to the manufacturer's protocol. The cultured Raw264.7 cells were harvested from the cell culture flask and stained with Cell Tracker-green (Invitrogen, USA) for 20 min at 37 °C. After washing, 0.5×10^5 cells were applied to the apical side of the BBB developed on nEBM after giving the OGD stress. A live cell imaging system was used with LSM980 microscope and images were captured at 20-s intervals for 30 min.

Statical Analysis. All data represent means (±s.e.m). The statistical analysis was determined using a t-test to compare two sets of data, and two-way analysis of variance (ANOVA) to compare in multiple groups;

*P < 0.05; **P < 0.01; ***P < 0.001; ****P < 0.0001). Prism 9 (GraphPad Software) was used for statistical analysis.

Author contributions

J.-W.C. and J.Y. designed and performed experiments, analyzed the data, and wrote the manuscript. D.S.K. and T.-E.P. provided insightful comments and supervised the overall project.

Declaration of competing interest

The authors declare that they have no known competing financial interests or personal relationships that could have appeared to influence the work reported in this paper.

Data availability

All data that support the findings of the study are included within the article and supplementary files.

Acknowledgements

This study was supported by a National Research Foundation of Korea (NRF) grant funded by the Ministry of Science and ICT (NRF-2020R1C1C1014753, 2019M3A9H1103769, and 2020R1A2B5B03002154), a grant of the Korea Health Technology R&D Project funded by the Ministry of Health & Welfare (HU20C009402), and a Research Fund (1.220023.01) of Ulsan National Institute of Science and Technology.

Appendix A. Supplementary data

Supplementary data to this article can be found online at https://doi.org/10.1016/j.biomaterials.2022.121983.

References

[1] C. Greene, M. Campbell, Tight junction modulation of the blood brain barrier: CNS delivery of small molecules, Tissue Barriers 4 (1) (2016), e1138017.
[2] N. Strazielle, J.F. Ghersi-Egea, Efflux transporters in blood-brain interfaces of the developing brain, Front. Neurosci. 9 (2015) 21.
[3] S. Aday, R. Cecchelli, D. Hallier-Vanuxeem, M. Dehouck, L. Ferreira, Stem cell-based human blood–brain barrier models for drug discovery and delivery, Trends Biotechnol. 34 (5) (2016) 382–393.
[4] C. Praça, S.C. Rosa, E. Sevin, R. Cecchelli, M.-P. Dehouck, L.S. Ferreira, Derivation of brain capillary-like endothelial cells from human pluripotent stem cell-derived endothelial progenitor cells, Stem Cell Rep. 13 (4) (2019) 599–611.
[5] E.S. Lippmann, S.M. Azarin, J.E. Kay, R.A. Nessler, H.K. Wilson, A. Al-Ahmad, S. P. Palecek, E.V. Shusta, Derivation of blood-brain barrier endothelial cells from human pluripotent stem cells, Nat. Biotechnol. 30 (8) (2012) 783–791.
[6] T.-E. Park, N. Mustafaoglu, A. Herland, R. Hasselkus, R. Mannix, E.A. FitzGerald, R. Prantil-Baun, A. Watters, O. Henry, M. Benz, Hypoxia-enhanced Blood-Brain Barrier Chip recapitulates human barrier function and shuttling of drugs and antibodies, Nat. Commun. 10 (1) (2019) 1–12.
[7] J.A. Brown, V. Pensabene, D.A. Markov, V. Allwardt, M.D. Neely, M. Shi, C. M. Britt, O.S. Hoilett, Q. Yang, B.M. Brewer, Recreating blood-brain barrier physiology and structure on chip: a novel neurovascular microfluidic bioreactor, Biomicrofluidics 9 (5) (2015), 054124.
[8] G.D. Vatine, R. Barrile, M.J. Workman, S. Sances, B.K. Barriga, M. Rahnama, S. Barthakur, M. Kasendra, C. Lucchesi, J. Kerns, N. Wen, W.R. Spivia, Z. Chen, J. Van Eyk, C.N. Svendsen, Human iPSC-derived blood-brain barrier chips enable disease modeling and personalized medicine applications, Cell Stem Cell 24 (6) (2019) 995–1005 e6.
[9] J. Yoo, T.H. Kim, S. Park, K. Char, S.H. Kim, J.J. Chung, Y. Jung, Use of elastic, porous, and ultrathin Co-culture membranes to control the endothelial barrier function via cell alignment, Adv. Funct. Mater. 31 (9) (2021), 2008172.
[10] R.N. Carter, S.M. Casillo, A.R. Mazzocchi, J.-P.S. DesOrmeaux, J.A. Roussie, T. R. Gaborski, Ultrathin transparent membranes for cellular barrier and co-culture models, Biofabrication 9 (1) (2017), 015019.
[11] D. Hudecz, T. Khire, H.L. Chung, L. Adumeau, D. Glavin, E. Luke, M.S. Nielsen, K. A. Dawson, J.L. McGrath, Y. Yan, Ultrathin silicon membranes for in situ optical analysis of nanoparticle translocation across a human blood–brain barrier model, ACS Nano 14 (1) (2020) 1111–1122.
[12] W. Halfter, P. Oertle, C.A. Monnier, L. Camenzind, M. Reyes-Lua, H. Hu, J. Candiello, A. Labilloy, M. Balasubramani, P.B. Henrich, New concepts in basement membrane biology, FEBS J. 282 (23) (2015) 4466–4479.
[13] A. Pozzi, P.D. Yurchenco, R.V. Iozzo, The nature and biology of basement membranes, Matrix Biol. 57 (2017) 1–11.
[14] J. Candiello, M. Balasubramani, E.M. Schreiber, G.J. Cole, U. Mayer, W. Halfter, H. Lin, Biomechanical properties of native basement membranes, FEBS J. 274 (11) (2007) 2897–2908.
[15] S. Van Helvert, C. Storm, P. Friedl, Mechanoreciprocity in cell migration, Nat. Cell Biol. 20 (1) (2018) 8–20.
[16] H. Li, Y. Zheng, Y.L. Han, S. Cai, M. Guo, Nonlinear elasticity of biological basement membrane revealed by rapid inflation and deflation, Proc. Natl. Acad. Sci. U. S. A. 118 (11) (2021).
[17] A. Glentis, P. Oertle, P. Mariani, A. Chikina, F. El Marjou, Y. Attieh, F. Zaccarini, M. Lae, D. Loew, F. Dingli, Cancer-associated fibroblasts induce metalloprotease-independent cancer cell invasion of the basement membrane, Nat. Commun. 8 (1) (2017) 1–13.
[18] G. Bhave, S. Colon, N. Ferrell, The sulfilimine cross-link of collagen IV contributes to kidney tubular basement membrane stiffness, Am. J. Physiol. Ren. Physiol. 313 (3) (2017) F596–F602.
[19] G. Fabris, A. Lucantonio, N. Hampe, E. Noetzel, B. Hoffmann, A. DeSimone, R. Merkel, Nanoscale topography and poroelastic properties of model tissue breast gland basement membranes, Biophys. J. 115 (9) (2018) 1770–1782.
[20] J. Crest, A. Diz-Muñoz, D.-Y. Chen, D.A. Fletcher, D. Bilder, Organ sculpting by patterned extracellular matrix stiffness, Elife 6 (2017), e24958.
[21] J.A. Last, S.J. Liliensiek, P.F. Nealey, C.J. Murphy, Determining the mechanical properties of human corneal basement membranes with atomic force microscopy, J. Struct. Biol. 167 (1) (2009) 19–24.
[22] R.N. Palchesko, J.L. Funderburgh, A.W. Feinberg, Engineered basement membranes for regenerating the corneal endothelium, Adv. Healthc. Mater. 5 (22) (2016) 2942–2950.
[23] T. Tilling, D. Korte, D. Hoheisel, H.J. Galla, Basement membrane proteins influence brain capillary endothelial barrier function in vitro, J. Neurochem. 71 (3) (1998) 1151–1157.
[24] A. Bosworth, H. Kim, K. O'Grady, I. Richter, L. Lee, B. O'Grady, E. Lippmann, Influence of Substrate Stiffness on Barrier Function in an iPSC-Derived in Vitro Blood-Brain Barrier Model, bioRxiv, 2021.
[25] L.L. Bischel, P.N. Coneski, J.G. Lundin, P.K. Wu, C.B. Giller, J. Wynne, B. R. Ringeisen, R.K. Pirlo, Electrospun gelatin biopapers as substrate for in vitro bilayer models of blood− brain barrier tissue, J. Biomed. Mater. Res. 104 (4) (2016) 901–909.
[26] D. Qi, S. Wu, H. Lin, M.A. Kuss, Y. Lei, A. Krasnoslobodtsev, S. Ahmed, C. Zhang, H. J. Kim, P. Jiang, Establishment of a human iPSC-and nanofiber-based microphysiological blood–brain barrier system, ACS Appl. Mater. Interfaces 10 (26) (2018) 21825–21835.
[27] M.E. Katt, R.M. Linville, L.N. Mayo, Z.S. Xu, P.C. Searson, Functional brain-specific microvessels from iPSC-derived human brain microvascular endothelial cells: the role of matrix composition on monolayer formation, Fluids Barriers CNS 15 (1) (2018) 1–12.
[28] P. Motallebnejad, S.M. Azarin, Chemically defined human vascular laminins for biologically relevant culture of hiPSC-derived brain microvascular endothelial cells, Fluids Barriers CNS 17 (1) (2020) 1–16.
[29] E. Gordon, L. Schimmel, M. Frye, The importance of mechanical forces for in vitro endothelial cell biology, Front. Physiol. 11 (2020) 684.
[30] P.P. Partyka, G.A. Godsey, J.R. Galie, M.C. Kosciuk, N.K. Acharya, R.G. Nagele, P. A. Galie, Mechanical stress regulates transport in a compliant 3D model of the blood-brain barrier, Biomaterials 115 (2017) 30–39.
[31] S. Seo, S.Y. Nah, K. Lee, N. Choi, H.N. Kim, Triculture model of in vitro BBB and its application to study BBB-associated chemosensitivity and drug delivery in glioblastoma, Adv. Funct. Mater. (2021), 2106860.
[32] G.N. Grifno, A.M. Farrell, R.M. Linville, D. Arevalo, J.H. Kim, L. Gu, P.C. Searson, Tissue-engineered blood-brain barrier models via directed differentiation of human induced pluripotent stem cells, Sci. Rep. 9 (1) (2019) 1–13.
[33] E. De Jong, D.S. Williams, L.K. Abdelmohsen, J.C. Van Hest, I.S. Zuhorn, A filter-free blood-brain barrier model to quantitatively study transendothelial delivery of nanoparticles by fluorescence spectroscopy, J. Contr. Release 289 (2018) 14–22.
[34] E.S. Lippmann, S.M. Azarin, J.E. Kay, R.A. Nessler, H.K. Wilson, A. Al-Ahmad, S. P. Palecek, E.V. Shusta, Derivation of blood-brain barrier endothelial cells from human pluripotent stem cells, Nat. Biotechnol. 30 (8) (2012) 783–791.
[35] F. Martino, A.R. Perestrelo, V. Vinarský, S. Pagliari, G. Forte, Cellular mechanotransduction: from tension to function, Front. Physiol. 9 (2018) 824.
[36] X. Cao, E. Ban, B.M. Baker, Y. Lin, J.A. Burdick, C.S. Chen, V.B. Shenoy, Multiscale model predicts increasing focal adhesion size with decreasing stiffness in fibrous matrices, Proc. Natl. Acad. Sci. U. S. A. 114 (23) (2017) E4549–E4555.
[37] Y. Hou, L. Yu, W. Xie, L.C. Camacho, M. Zhang, Z. Chu, Q. Wei, R. Haag, Surface roughness and substrate stiffness synergize to drive cellular mechanoresponse, Nano Lett. 20 (1) (2020) 748–757.
[38] S.R. Peyton, A.J. Putnam, Extracellular matrix rigidity governs smooth muscle cell motility in a biphasic fashion, J. Cell. Physiol. 204 (1) (2005) 198–209.
[39] K. Shen, H. Kenche, H. Zhao, J. Li, J. Stone, The role of extracellular matrix stiffness in regulating cytoskeletal remodeling via vinculin in synthetic smooth muscle cells, Biochem. Biophys. Res. Commun. 508 (1) (2019) 302–307.
[40] A.A. Birukova, A.S. Shah, Y. Tian, N. Moldobaeva, K.G. Birukov, Dual role of vinculin in barrier-disruptive and barrier-enhancing endothelial cell responses, Cell. Signal. 28 (6) (2016) 541–551.

[41] D.W. Zhou, T.T. Lee, S. Weng, J. Fu, A.J. García, Effects of substrate stiffness and actomyosin contractility on coupling between force transmission and vinculin–paxillin recruitment at single focal adhesions, Mol. Biol. Cell 28 (14) (2017) 1901–1911.
[42] N.V. Bogatcheva, A.D. Verin, Reprint of "The role of cytoskeleton in the regulation of vascular endothelial barrier function"[Microvascular Research 76 (2008) 202–207], Microvasc. Res. 77 (1) (2009) 64–69.
[43] A. Shakhov, V. Dugina, I. Alieva, Structural features of actin cytoskeleton required for endotheliocyte barrier function, Biochemistry (Moscow) 84 (4) (2019) 358–369.
[44] N. Prasain, T. Stevens, The actin cytoskeleton in endothelial cell phenotypes, Microvasc. Res. 77 (1) (2009) 53–63.
[45] W.M. Pardridge, The blood-brain barrier: bottleneck in brain drug development, NeuroRx 2 (1) (2005) 3–14.
[46] D. Gomez-Zepeda, M. Taghi, J.-M. Scherrmann, X. Decleves, M.-C. Menet, ABC transporters at the blood–brain interfaces, their study models, and drug delivery implications in gliomas, Pharmaceutics 12 (1) (2020) 20.
[47] W. Löscher, H. Potschka, Blood-brain barrier active efflux transporters: ATP-binding cassette gene family, NeuroRx 2 (1) (2005) 86–98.
[48] R. Ito, K. Umehara, S. Suzuki, K. Kitamura, K.-i. Nunoya, Y. Yamaura, H. Imawaka, S. Izumi, N. Wakayama, T. Komori, A human immortalized cell-based blood–brain barrier triculture model: development and characterization as a promising tool for Drug− brain permeability studies, Mol. Pharm. 16 (11) (2019) 4461–4471.
[49] E.S. Lippmann, A. Al-Ahmad, S.M. Azarin, S.P. Palecek, E.V. Shusta, A retinoic acid-enhanced, multicellular human blood-brain barrier model derived from stem cell sources, Sci. Rep. 4 (1) (2014) 1–10.
[50] M. Ohshima, S. Kamei, H. Fushimi, S. Mima, T. Yamada, T. Yamamoto, Prediction of drug permeability using in vitro blood–brain barrier models with human induced pluripotent stem cell-derived brain microvascular endothelial cells, BioResearch Open Access 8 (1) (2019) 200–209.
[51] L. Delsing, P. Dönnes, J. Sánchez, M. Clausen, D. Voulgaris, A. Falk, A. Herland, G. Brolén, H. Zetterberg, R. Hicks, Barrier properties and transcriptome expression in human iPSC-derived models of the blood–brain barrier, Stem Cell. 36 (12) (2018) 1816–1827.
[52] L. Cucullo, M. Hossain, V. Puvenna, N. Marchi, D. Janigro, The role of shear stress in Blood-Brain Barrier endothelial physiology, BMC Neurosci. 12 (1) (2011) 1–15.
[53] L.M. Tai, A.J. Loughlin, D.K. Male, I.A. Romero, P-glycoprotein and breast cancer resistance protein restrict apical-to-basolateral permeability of human brain endothelium to amyloid-β, J. Cerebr. Blood Flow Metabol. 29 (6) (2009) 1079–1083.
[54] S.E. Lakhan, A. Kirchgessner, D. Tepper, L. Aidan, Matrix metalloproteinases and blood-brain barrier disruption in acute ischemic stroke, Front. Neurol. 4 (2013) 32.
[55] K. Nian, I.C. Harding, I.M. Herman, E.E. Ebong, Blood-brain barrier damage in ischemic stroke and its regulation by endothelial mechanotransduction, Front. Physiol. 11 (2020) 1681.
[56] S. Bernardo-Castro, J.A. Sousa, A. Brás, C. Cecília, B. Rodrigues, L. Almendra, C. Machado, G. Santo, F. Silva, L. Ferreira, Pathophysiology of blood–brain barrier permeability throughout the different stages of ischemic stroke and its implication on hemorrhagic transformation and recovery, Front. Neurol. (2020) 1605.
[57] S. Page, S. Raut, A. Al-Ahmad, Oxygen-glucose deprivation/reoxygenation-induced barrier disruption at the human blood–brain barrier is partially mediated through the HIF-1 pathway, NeuroMolecular Med. 21 (4) (2019) 414–431.
[58] I. Arbeláez-Quintero, M. Palacios, To Use or Not to Use Metformin in Cerebral Ischemia: a Review of the Application of Metformin in Stroke Rodents, Stroke Research and Treatment 2017, 2017.
[59] Y. Farbood, A. Sarkaki, L. Khalaj, F. Khodagholi, M. Badavi, G. Ashabi, Targeting adenosine monophosphate-activated protein kinase by metformin adjusts post-ischemic hyperemia and extracellular neuronal discharge in transient global cerebral ischemia, Microcirculation 22 (7) (2015) 534–541.
[60] H. Kadry, B. Noorani, U. Bickel, T.J. Abbruscato, L. Cucullo, Comparative assessment of in vitro BBB tight junction integrity following exposure to cigarette smoke and e-cigarette vapor: a quantitative evaluation of the protective effects of metformin using small-molecular-weight paracellular markers, Fluids Barriers CNS 18 (1) (2021) 1–15.
[61] A.L. McCall, A.M. Van Bueren, V. Nipper, M. Moholt-Siebert, H. Downes, N. Lessov, Forebrain ischemia increases GLUT1 protein in brain microvessels and parenchyma, J. Cerebr. Blood Flow Metabol. 16 (1) (1996) 69–76.
[62] I. Alquisiras-Burgos, P. Aguilera, Involvement of glucose transporter overexpression in the protection or damage after ischemic stroke, Neural Regenerat. Res. 17 (4) (2022) 783.
[63] A.E. Sifat, B. Vaidya, M.A. Kaisar, L. Cucullo, T.J. Abbruscato, Nicotine and electronic cigarette (E-Cig) exposure decreases brain glucose utilization in ischemic stroke, J. Neurochem. 147 (2) (2018) 204–221.
[64] B. Choi, J.W. Choi, H. Jin, H.R. Sim, J.H. Park, T.E. Park, J.H. Kang, Condensed ECM-based nanofilms on highly permeable PET membranes for robust cell-to-cell communications with improved optical clarity, Biofabrication 13 (4) (2021).
[65] M.E. Katt, R.M. Linville, L.N. Mayo, Z.S. Xu, P.C. Searson, Functional brain-specific microvessels from iPSC-derived human brain microvascular endothelial cells: the role of matrix composition on monolayer formation, Fluids Barriers CNS 15 (1) (2018) 7.
[66] V.S. LeBleu, B. Macdonald, R. Kalluri, Structure and function of basement membranes, Exp. Biol. Med. 232 (9) (2007) 1121–1129.
[67] Y. Li, Z.Y. Zhu, T.T. Huang, Y.X. Zhou, X. Wang, L.Q. Yang, Z.A. Chen, W.F. Yu, P. Y. Li, The peripheral immune response after stroke-A double edge sword for blood-brain barrier integrity, CNS Neurosci. Ther. 24 (12) (2018) 1115–1128.
[68] F. Rohde, K. Danz, N. Jung, S. Wagner, M. Windbergs, Electrospun scaffolds as cell culture substrates for the cultivation of an in vitro blood–brain barrier model using human induced pluripotent stem cells, Pharmaceutics 14 (6) (2022) 1308.
[69] K. Huang, A.D. Castiaux, R. Podicheti, D.B. Rusch, R.S. Martin, L.A. Baker, A hybrid nanofiber/paper cell culture platform for building a 3D blood–brain barrier model, Small Methods 5 (9) (2021), 2100592.
[70] J.G. DeStefano, J.J. Jamieson, R.M. Linville, P.C. Searson, Benchmarking in vitro tissue-engineered blood–brain barrier models, Fluids Barriers CNS 15 (1) (2018) 1–15.
[71] M. Campisi, Y. Shin, T. Osaki, C. Hajal, V. Chiono, R.D. Kamm, 3D self-organized microvascular model of the human blood-brain barrier with endothelial cells, pericytes and astrocytes, Biomaterials 180 (2018) 117–129.
[72] A.L. Placone, P.M. McGuiggan, D.E. Bergles, H. Guerrero-Cazares, A. Quinones-Hinojosa, P.C. Searson, Human astrocytes develop physiological morphology and remain quiescent in a novel 3D matrix, Biomaterials 42 (2015) 134–143.
[73] H. Aoki, M. Yamashita, T. Hashita, T. Iwao, T. Matsunaga, Laminin 221 fragment is suitable for the differentiation of human induced pluripotent stem cells into brain microvascular endothelial-like cells with robust barrier integrity, Fluids Barriers CNS 17 (1) (2020) 1–11.
[74] J. Di Russo, A.L. Luik, L. Yousif, S. Budny, H. Oberleithner, V. Hofschröer, J. Klingauf, E. van Bavel, E.N. Bakker, P. Hellstrand, Endothelial basement membrane laminin 511 is essential for shear stress response, EMBO J. 36 (2) (2017) 183–201.
[75] K. Kangwantas, E. Pinteaux, J. Penny, The extracellular matrix protein laminin-10 promotes blood–brain barrier repair after hypoxia and inflammation in vitro, J. Neuroinflammation 13 (1) (2016) 1–12.
[76] J. Gautam, X. Zhang, Y. Yao, The role of pericytic laminin in blood brain barrier integrity maintenance, Sci. Rep. 6 (2016), 36450.
[77] M.S. Thomsen, S. Birkelund, A. Burkhart, A. Stensballe, T. Moos, Synthesis and deposition of basement membrane proteins by primary brain capillary endothelial cells in a murine model of the blood-brain barrier, J. Neurochem. 140 (5) (2017) 741–754.
[78] D.N. Rockwood, R.C. Preda, T. Yucel, X. Wang, M.L. Lovett, D.L. Kaplan, Materials fabrication from Bombyx mori silk fibroin, Nat. Protoc. 6 (10) (2011) 1612–1631.
[79] D. Kim, S.J. Lee, J. Youn, H. Hong, S. Eom, D.S. Kim, A Deep and Permeable Nanofibrous Oval-Shaped Microwell Array for Stable Formation of Viable and Functional Spheroids, Biofabrication, 2021.
[80] M. Ahearne, Y. Yang, A.J. El Haj, K.Y. Then, K.-K. Liu, Characterizing the viscoelastic properties of thin hydrogel-based constructs for tissue engineering applications, J. R. Soc. Interface 2 (5) (2005) 455–463.
[81] J.B. van Bree, A.G. de Boer, M. Danhof, L.A. Ginsel, D.D. Breimer, Characterization of an "in vitro" blood-brain barrier: effects of molecular size and lipophilicity on cerebrovascular endothelial transport rates of drugs, J. Pharmacol. Exp. Therapeut. 247 (3) (1988) 1233–1239.
[82] D. Kim, S. Eom, S.M. Park, H. Hong, D.S. Kim, A collagen gel-coated, aligned nanofiber membrane for enhanced endothelial barrier function, Sci. Rep. 9 (1) (2019) 1–11.
[83] J. Karlsson, P. Artursson, A method for the determination of cellular permeability coefficients and aqueous boundary layer thickness in monolayers of intestinal epithelial (Caco-2) cells grown in permeable filter chambers, Int. J. Pharm. 71 (1–2) (1991) 55–64.